Journal of Materials Chemistry A

PAPER

Durability of $La_{0.20}Sr_{0.25}Ca_{0.45}TiO_3$-based SOFC anodes: identifying sources of degradation in Ni and Pt/ceria co-impregnated fuel electrode microstructures

Robert Price,*[a] Ueli Weissen [b], Jan G. Grolig [b], Mark Cassidy [a], Andreas Mai [b] and John T. S. Irvine [a]

Solid oxide fuel cells (SOFC) comprising LSM-YSZ/LSM composite cathodes, 6ScSZ electrolytes and $La_{0.20}Sr_{0.25}Ca_{0.45}TiO_3$ (LSCT$_{A-}$) anode 'backbone' microstructures were prepared using thick-film ceramic processing techniques. Activation and decoration of the LSCT$_{A-}$ anode 'backbone' with electrocatalytic coatings of cerium-based oxides and metallic Ni or Pt particles was achieved using the technique of catalyst co-impregnation. SOFC containing Ni/CGO, Ni/CeO$_2$ and Pt/CGO impregnated LSCT$_A$ anodes were tested up to ~1000 hours by the Swiss SOFC manufacturer: HEXIS, under realsitic operating conditions, including 15 redox, thermo and thermoredox cycles. The voltage degradation rates observed over the entire test period for the SOFC containing the Ni/CGO, Ni/CeO$_2$ and Pt/CGO impregnated LSCT$_{A-}$ anodes were 14.9 %, 7.7 % and 13.4 %, respectively. Post-mortem microscopic analyses indicated that CeO$_2$ formed ubiquitous coatings upon the LSCT$_{A-}$ anode microstructure, allowing retention of a high population density of metallic (Ni) particles, whilst CGO formed 'islands' upon the microstructure and some agglomerates within the pores, leading to more facile agglomeration of metallic (Ni and Pt) nanoparticles. Correlation of the post-mortem microscopy with AC impedance analysis revealed that the agglomeration of metallic catalyst resulted in an increase in the high-frequency anode polarisation resistance, whilst agglomeration of the ceria-based component directly resulted in the development of a low-frequency process that may be attributed to combined contributions from gas conversion and chemical capacitance.

Introduction

Solid Oxide Fuel Cells (SOFC) are electrochemical energy conversion devices which allow cleaner heat and electricity generation to occur at much higher efficiencies than can be achieved using fuel combustion methods. [1] Due to the employment of a solid oxide electrolyte, SOFC must be operated at temperatures above 600 °C in order to allow oxide anion migration from the cathode to the anode. [2] Therefore, by carrying out this exothermic fuel oxidation at higher temperatures, high-quality heat is generated, alongside electricity, which can be recovered and utilised effectively. This simultaneous generation of heat and electricity makes these devices ideal for use in combined heat and power (CHP) applications. [3,4]

The current state-of-the-art SOFC anode material is the Ni-based ceramic-metal composite (cermet). The most commonly used cermets comprise a structural Ni component, in addition to a structural oxide-ion conducting ceramic component, *e.g.* cerium gadolinium oxide (CGO) or yttria-stabilised-zirconia (YSZ). Until now, the Ni-based cermets have been shown preference for their high activity towards electrochemical oxidation of fuels, such as H$_2$ or syngas, high ionic and electronic

conductivities and matching thermal expansion coefficients to other cell components. [5] Unfortunately, though, when used with an unprocessed, hydrocarbon-containing fuel gas, this material undergoes coking, [5] irreversible sulphur poisoning (by naturally occurring H$_2$S and odourising agents), [5] as well as structural rearrangement and failure due to redox instability. [6,7] Therefore, a novel replacement anode material is required in order to address the shortcomings of the Ni-based cermets and improve the flexibility and resilience of SOFC anodes to varying compositions and qualities of fuel gases, for use in next generation SOFC systems.

In order to mitigate some of the complications that arise due to the use of a structural Ni phase in these anode materials, [7–10] a conductive ceramic anode 'backbone' microstructure may be decorated with electrocatalytically active species using the process of catalyst impregnation. This technique, and related techniques such as dip coating and wash coating, have been employed successfully for many decades in the preparation of monoliths for automotive catalytic converters (i.e. cordierite monoliths coated in CeO$_2$ and Noble metals). [11] However, Craciun *et al.* realised that it could also be used to prepare SOFC electrode microstructures. [12] Here, precursor solutions (typically containing nitrate salts of the desired catalyst phases) are added to the pre-sintered, porous anode microstructures to deposit coatings and particles of electrocatalyst precursors, before being calcined to form the required phases. As a result, impregnation of a wide variety of ceramic anode 'backbone'

a. *School of Chemistry, University of St Andrews, St Andrews, Fife, KY16 9ST, United Kingdom.*
b. *HEXIS AG, Zum Park 5, CH-8404 Winterthur, Switzerland.*

materials has been carried out, for >15 years, in both academic [12–18] and industrial research. [16,19,20]

The A-site deficient perovskite $La_{0.20}Sr_{0.25}Ca_{0.45}TiO_3$ ($LSCT_{A–}$) is a mixed ionic and electronic conductor (MIEC) material, which has shown particular promise as a replacement anode 'backbone' material for the Ni-based cermet, due to its high 'effective' electrical conductivity under reducing conditions (17 S cm^{-1} at 850 °C and $p(O_2)$ = 10^{-19} atm), for this class of perovskite. [21,22] When impregnated with $Ce_{0.80}Gd_{0.20}O_{1.90}$ (CGO) and Ni electrocatalysts, highly active electrode nanostructures were produced, which showed encouraging performance during both button cell scale tests and larger scale industrial tests at HEXIS. [16,19] Despite the good initial performances observed during short stack and full system testing at HEXIS, substantial degradation occurred due to non-optimal anode microstructures and agglomeration of Ni catalyst particles. [19]

Second generation research into these co-impregnated $LSCT_{A–}$ anode systems involved the successful re-optimisation of the $LSCT_{A–}$ microstructure, for catalyst impregnation, gas diffusion and high effective electrical conductivity, as well as an exploration of a variety of impregnated catalyst systems, *e.g.* Ni/CGO, Pd/CGO, Pt/CGO, Rh/CGO and Ru/CGO, which showed substantial improvements in performance over the previous generation of research. [21,23,24] Furthermore, optimisation and upscaling of the Rh/CGO co-impregnated $LSCT_{A-}$ anode to short stack scales at HEXIS has given rise to 'all-oxide' SOFC that rival voltage degradation rates of the current state-of-the-art anode, whilst offering high redox/thermo/thermoredox cycling stability, the ability to operate in sulfur-laden fuel gas and overload stability. [25]

In this research, an exploration of the stability of Ni catalyst particles was undertaken, as this catalyst is known to degrade more rapidly than platinum group metals, due to its mobility under reducing conditions, even in impregnated SOFC anodes. Long-term test data is presented for SOFC containing: i) a Ni/CGO impregnated $LSCT_{A–}$ anode and ii) a Ni/CeO$_2$ impregnated $LSCT_{A–}$ anode in order to evaluate the effect of the ceria-based component in 'anchoring' and stabilising the Ni particles on the anode 'backbone', under realistic operating conditions (i.e. under redox, thermo and thermoredox cycling treatments). Subsequently, in order to evaluate the impact of the metallic catalyst component on the durability and behaviour of these nanostructured anodes, a SOFC containing a Pt/CGO impregnated $LSCT_{A–}$ anode was tested under the same conditions. AC impedance spectroscopy was used to identify rate limiting processes occurring within the SOFC and temporal changes in spectra are correlated to the features observed during post-mortem electron microscopic analysis of the SOFC anodes.

Experimental

$La_{0.20}Sr_{0.25}Ca_{0.45}TiO_3$ ($LSCT_{A–}$) powder, supplied by Treibacher Industrie AG, was incorporated into a 75 weight % (wt. %) solids loading ink, as previously reported, [21,23] and screen printed onto 160 µm thick 6 molar % scandia-stabilised zirconia (6ScSZ) electrolyte supports (HEXIS) using a 230 mesh count (per inch)

screen with a 1 cm^2 square print geometry. Subsequently, the anodes were dried at 80 °C to evaporate the solvent from the green layer before being sintered at 1350 °C for 2 hours in air. $(La_{0.80}Sr_{0.20})_{0.95}MnO_3$ (LSM, Praxair Specialty Ceramics) and 8 mol. % yttria-stabilised zirconia (8YSZ, Daiichi Kigenso Kagaku Kogyo Co. Ltd) were incorporated into a 70 wt. % solids loading composite cathode ink, in a 50:50 wt. % ratio, whilst a 70 wt. % solids loading current collection ink was prepared from pure LSM. Functionalised cathodes were screen printed onto the opposite side of the 6ScSZ electrolyte support using a single layer of LSM-YSZ ink and a double layer of LSM ink. Cathodes were sintered at 1100 °C for 2 hours in air.

SOFC anode 'backbones' were then activated using the process of catalyst impregnation. Precursor solutions of CeO$_2$ and $Ce_{0.80}Gd_{0.20}O_{1.9}$ were prepared by dissolving $Ce(NO_3)_6 \cdot 6H_2O$ (99 %, Sigma-Aldrich) and the required molar ratios of $Ce(NO_3)_3 \cdot 6H_2O$ and $Gd(NO_3)_3 \cdot 6H_2O$ (99 %, Sigma-Aldrich), respectively, in ethanol to afford solutions of 0.5 mol dm^{-3} concentration. A droplet of solution was added to the $LSCT_{A–}$ 'backbone' and was allowed to diffuse into the microstructure, before the solvent was evaporated at 80 °C for 30 minutes. Subsequently, having coated the $LSCT_{A–}$ anode 'backbone' microstructure, the nitrate precursors were decomposed at 500 °C for 30 minutes in air. This process was repeated until the desired loading of CeO$_2$ or CGO was obtained, as a weight percentage of the $LSCT_{A–}$ anode mass. Also, a precursor solution of $Ni(NO_3)_3 \cdot 6H_2O$ was prepared to a 0.5 mol dm^{-3} concentration in ethanol and an acidic solution of $H_2Pt(NO_3)_4$ (Johnson-Matthey), diluted with ethanol, was used as the precursor for the Pt catalyst. The aforementioned procedure was then used to add the metallic catalyst phase to the $LSCT_{A–}$ anode.

A current collecting layer of Ni paste was added to the surface of the anodes and was allowed to dry before a Ni mesh was attached to the Ni paste layer. Current collectors for the cathodes comprised only Au mesh added to the electrode surface without the use of any contacting paste. SOFC were then placed into the lower part of an alumina cell housing, that contained a gas flow field designed to aid the distribution of fuel gas over the anode. Alumina felt gaskets were placed on either side of the electrolyte in order to cushion the SOFC from the cell housing and to allow the creation of a combustion zone around the edge of the cell, providing analogous test conditions to standard HEXIS SOFC button cells and larger scale SOFC stacks, which have a 'sealless' design. Subsequently, the upper part of the alumina cell housing was placed onto the cathode side of the SOFC to complete the installation. A schematic of the cell housing is published elsewhere. [10] SOFC were heated to 850 °C in air before a flow of 5 % H$_2$/95 % N$_2$ (forming gas) was fed to the anode compartment, to slowly introduce the reducing gas. Subsequently, a compressed air supply was fed to the cathode at 420 mL min^{-1} and non-humidified H$_2$ (99 % H$_2$/1 % H$_2$O at 25 °C) was introduced to the anode at a flow rate of 200 mL min^{-1}, whilst ceasing the flow of forming gas.

Initial characterisation of SOFC was performed using AC impedance spectroscopy at 900 °C, 875 °C, 850 °C, 825 °C and 800 °C, in order to observe the temperature dependence of rate limiting processes and to identify the processes contributing to

the polarisation resistance of the SOFC. Spectra were collected at 300 mA cm^{-2}, with an excitation amplitude of 10 mA. Also, current variation measurements were performed under current densities of 300 mA cm^{-2}, 250 mA cm^{-2}, 200 mA cm^{-2}, 150 mA cm^{-2} and 100 mA cm^{-2} at 850 °C, with the same excitation amplitude, in order to further assign temperature independent processes. 4-wire AC impedance spectroscopy was carried out using a Zahner-Elektrik IM6ex Impedance Spectrometer (Zahner-Elektrik GmbH & Co KG, Kronach, Germany). During long-term galvanostatic operation, SOFC were held at a current density of 300 mA cm^{-2} at 850 °C, which is relevant to the standard operation of HEXIS SOFC (that contain state-of-the-art Ni/CGO anodes). Redox cycling was performed by halting the flow of H$_2$ and allowing air to flow back into the anode chamber for 1-2 hours. This was typically accompanied by a temperature drop of approximately 15 °C, due to the extinction of the post-cell combustion zone. Subsequently, the H$_2$ flow to the anode chamber was reinstated to complete the redox cycle. Thermocycling involved rapidly decreasing the operating temperature from 850 °C to between 250°C and 200 °C whilst maintaining air flow to the cathode and forming gas flow to the anode, before re-establishing operating temperature, and thermoredox cycling involved the same rapid drop in temperature accompanied by the aforementioned redox cycling protocol.

Post-mortem scanning electron microscopy (SEM) was carried out on the fractured cross-sections of SOFC in order to provide micrographs of the overall anode microstructure and the arrangement of the nanostructure. Micrographs were obtained using a FEI Scios Dualbeam FIB-SEM (Focussed Ion Beam-SEM) (FEI Company, Hillsboro, Oregon, USA). Samples were not subjected to sputtering with a conductive coating, in order to prevent masking of metallic nanoparticles, thus, charging was avoided by the use of a low accelerating voltage (1 kV) for imaging. FIB-SEM was also used to prepare ion-milled cross sections of the impregnated anodes for scanning transmission electron microscopy (STEM). [26] STEM was employed to obtain high resolution and high magnification micrographs of impregnated Ni/Pt particles and ceria-based coatings resting upon the LSCT$_{A-}$ anode 'backbone' and energy dispersive analysis of X-rays (EDX) was used to confirm the identity of imaged components within the anode using a mapping function. STEM imaging was carried out using FEI Titan Themis 200 S/TEM and EDX mapping was performed using a Super-X high sensitivity windowless EDX detector (FEI Company, Hillsboro, Oregon, USA).

Results and Discussion

Characterisation of SOFC containing Ni/CGO and Ni/CeO₂ co-impregnated LSCT$_{A-}$ anodes

Long-term galvanostatic operation of the Ni/CGO and Ni/CeO₂ cells. Figures 1 and 2 provide a comparison of the evolution of performance of the SOFC containing the Ni/CGO impregnated LSCT$_{A-}$ anode (Ni/CGO cell) and Ni/CeO₂ impregnated LSCT$_{A-}$ anode (Ni/CeO₂ cell), respectively, under galvanostatic
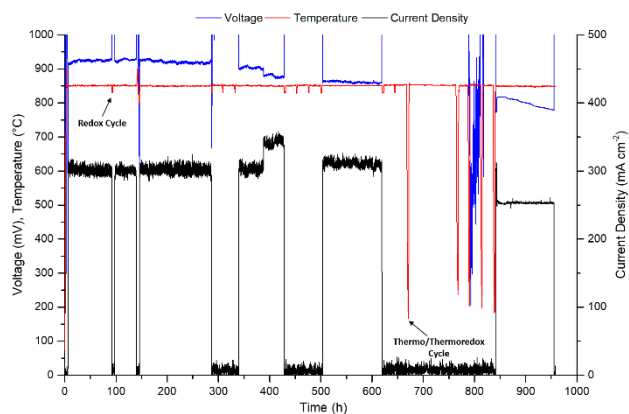

Figure 1. Long-term galvanostatic operation of the SOFC containing a Ni/CGO co-impregnated LSCT$_{A-}$ anode, including redox, thermo and thermoredox cycling treatments.

operation for a period of approximately 1000 hours. The Ni/CGO cell contained 14 wt. % CGO and 4 wt. % Ni, whilst the Ni/CeO₂ cell contained 14 wt. % CeO₂ and 5 wt. % Ni. Firstly, it is important to note that some issues with the stability of the current sink were experienced whilst testing the Ni/CGO cell, thus the requested current of 300 mA cm^{-2} was not achieved during some periods of operation. The current trace for the Ni/CeO₂ cell is clearly much more stable. Despite this, the voltage degradation rates calculated throughout the entire period of operation were 14.9 % and 7.7 % for the Ni/CGO cell and the Ni/CeO₂ cell, respectively. Considering the degradation in terms of ASR, the Ni/CGO cell showed an increase of 290 mΩ cm^2, whilst the Ni/CeO₂ cell showed an increase of 170 mΩ cm^2. For ease of comparison, voltage and resistance degradation values for all SOFC examined in this manuscript have been summarised in table S1, which may be found in the supplementary information file. During the course of the first 3000 hours of testing, the 6ScSZ electrolyte is known to degrade by 80 mΩ cm^2, [27] under these test conditions. Therefore, the contribution of electrolyte degradation over the ~1000 hour period (~50 mΩ cm^2) must be acknowledged, however, in the case of the Ni/ceria-based co-impregnated catalyst systems, this is a relatively minor contribution. Surprisingly, the Ni/CGO cell, which did not operate under current for large proportions of the test period, degraded almost twice as much as the Ni/CeO₂ cell, which degraded at a constant rate. This was somewhat unexpected as operation at high temperature under open circuit voltage (OCV), or hot-idle conditions, is not believed to be detrimental to performance.

As Ni is known to be mobile in both cermet and impregnated nanoparticular systems, it is a challenge to 'anchor' these particles to prevent/minimise agglomeration and degradation over time. Therefore, the difference in degradation rate achieved by altering the composition of the ceria-based component implies that the mobility of Ni nanoparticles may be controlled by the mutualistic and stabilising relationship between the metallic component and the ceria-based component in these impregnated anode catalyst systems. A mutualistic relationship between Ni and CeO₂ was reported by Verbraeken *et al.* [16] in a previous generation of this research, in terms of increased electrocatalytic activity for H$_2$ oxidation,
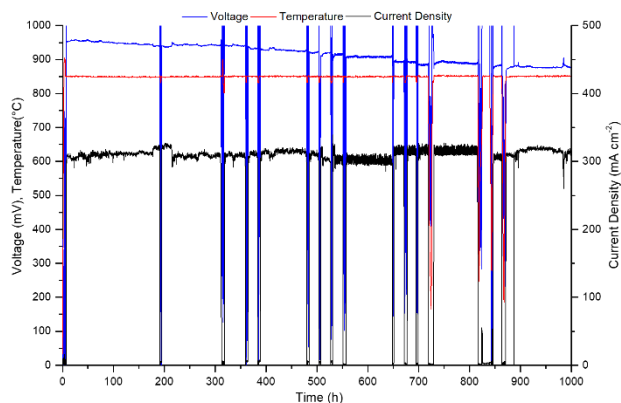
Figure 2. Long-term galvanostatic operation of the SOFC containing a Ni/CeO$_2$ co-impregnated LSCT$_{A-}$ anode, including redox, thermo and thermoredox cycling treatments.

further implying that the presence and composition of the ceria-based component is crucial to the performance of these impregnated anode catalysts.

Both SOFC were subjected to ten redox cycles and four or five thermo or thermoredox cycles throughout the operational periods. Examples of redox and thermo/thermoredox cycling events are shown in figure 1. The data presented in figure 1 shows that the first redox cycle has little effect on the operating voltage of the Ni/CGO cell and the initial ~285 hour period of operation results in a steady rate of degradation. However, further redox cycling, during periods of hot-idle operation, results in different degradation behaviours. For example, during the period of operation between 285 hours and 340 hours, three redox cycles were carried out. When the current density of 300 mA cm^{-2} was restored at 340 hours, the operating voltage appears to have degraded at a similar rate to that observed during the first 285 hours of operation. However, the unexpected rise of current density to 350 mA cm^{-2} causes a decrease in operating voltage and the subsequent period of hot-idle operation, between 428 hours and 504 hours (including a further four redox cycles), resulted in an accelerated rate of degradation. This is evidenced by the large drop in operating voltage (13 mV) over the course of only 116 hours (388 - 504 hours). The degradation rate observed at 300 mA cm^{-2} between 504 hours and 620 hours appears to stabilise and, once again, shows a similar gradient to the operating voltage profile collected during the first 285 hours operation. Unfortunately, after 620 hours of testing, further issues with the current sink led to a 222 hour period of operation without load. During this period two final redox cycles were carried out, followed by a single thermocycle (at 668 hours) and four thermoredox cycles (between 764 hours and 841 hours). The erratic nature of the voltage response observed during thermoredox cycling indicates that current collection at the electrodes began to deteriorate and, when a current of 250 mA cm^{-2} was drawn from the cell, continuous and severe degradation of the cell was observed, indicating structural failure of the cell (i.e. crack formation). Therefore, the test period was terminated at 958 hours and post-mortem examination of the Ni/CGO cell confirmed that a crack, propagating from the electrolyte into

the active area of the SOFC, was responsible for the accelerated degradation towards the end of the test period.

Considering figure 2, the current density drawn from the Ni/CeO$_2$ cell was comparatively much more stable than for the Ni/CGO cell. Ten redox cycles were performed between 198 and 695 hours and it is possible to conclude that the degradation directly resulting from redox cycling is minimal. In fact, as observed for the Ni/CGO cell it is actually periods of operation under slightly higher current density which result in accelerated degradation of voltage. For the Ni/CeO$_2$ cell, only four thermoredox cycles were performed, between 813 and 884 hours. In contrast to the Ni/CGO cell, the Ni/CeO$_2$ cell responds well to thermoredox cycling and degradation does not accelerate as a result of these treatments. A ~30 hour period of hot-idle operation ensued at 816 hours, due to instability of the current sink. However, upon re-establishment of operating conditions, performance recovered without signs of detriment, reinforcing the assumption that hot-idle operation is not detrimental to these co-impregnated LSCT$_{A-}$ anodes. Finally, after the fourth thermoredox cycle, galvanostatic operation resumed until the end of the operational period (1006 hours) and stable performance (specifically voltage degradation) was observed.

In figures 1 and 2, it is possible to see that voltage degradation begins before redox cycling has been performed, for both cells. Therefore, there is an underlying degradation mechanism that is independent of different redox cycling treatments, but is affected by the current density drawn from the SOFC. This is supported by previous research (at HEXIS) into the redox stability of SOFC containing Ni-YSZ and Ni-CG40 (Ce$_{0.6}$Gd$_{0.4}$O$_{2-\delta}$) cermets, which revealed the high redox stability of CG40-containing anodes during a period of operation at 850 °C and OCV, including 8 redox cycles. [10] During this period, the ASR only increased by 30 mΩ cm^2 for the Ni-CG40 anode, mainly due to degradation in the polarisation resistance, whilst the Ni-YSZ anode exhibited a degradation of 108 mΩ cm^2. [10] Therefore, in these Ni/ceria co-impregnated LSCT$_{A-}$ anodes, degradation is thought to relate to agglomeration of the Ni nanoparticles, into much larger Ni particles, at the expense of available surface area for oxidation of H$_2$. Thus, the difference in degradation rates observed is a function of the extent of agglomeration of Ni, which is controlled by the interaction between the Ni catalyst particles and the underlying ceria-based component, *i.e.* how stabilising different compositions of doped-ceria are to the Ni particles.

AC impedance spectroscopic analysis of the Ni/CGO and Ni/CeO$_2$ cells. In order to identify the performance limiting processes within these SOFC, AC impedance spectroscopy was carried out under operating conditions. Initial spectra were collected at 850 °C, as a function of current density, at the start of the test period, for both cells. Subsequently, a second set of spectra was collected, using the same conditions, after one redox cycle had been performed, in order to assess the impact on anode related processes. Figures 3a and b show the complex plane AC impedance data for the Ni/CGO cell, before and after
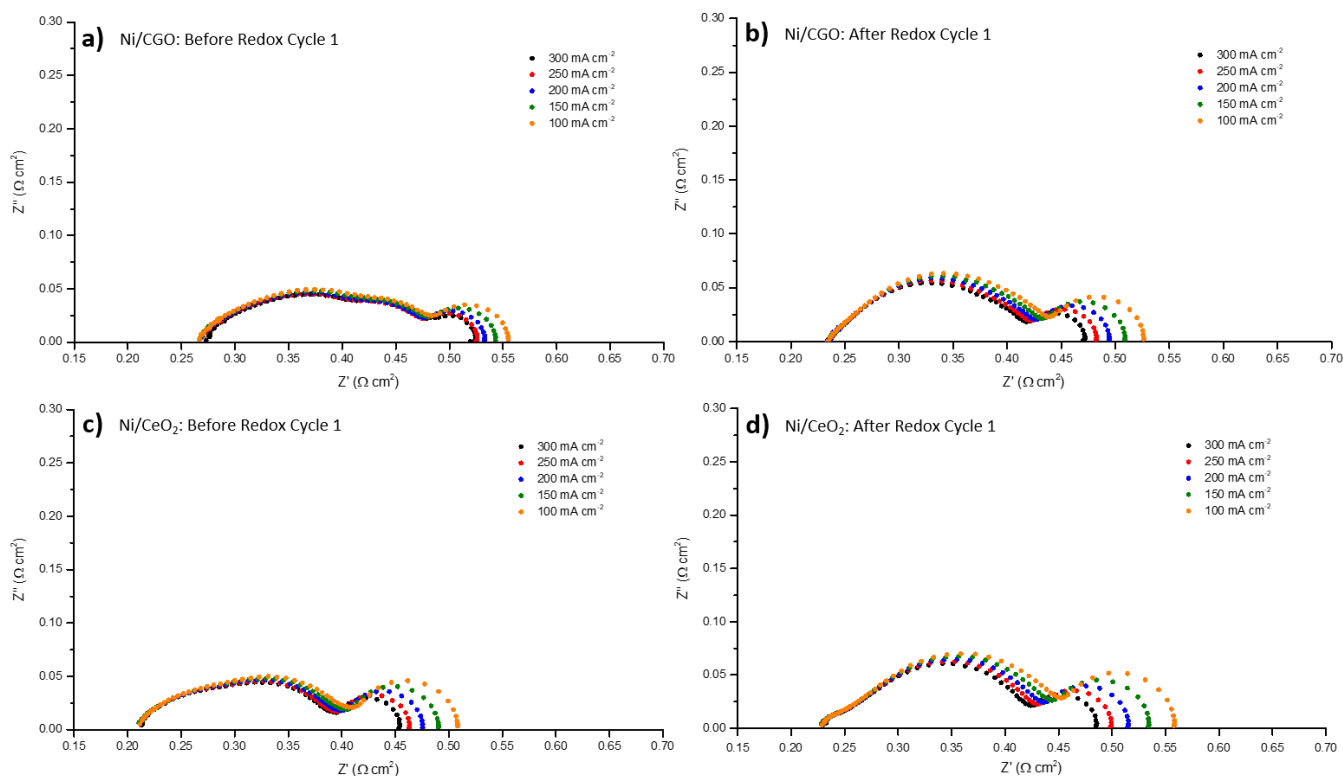
PAPER

Figure 3. Complex plane AC impedance spectra collected at 850 °C as a function of current density for the SOFC containing: a) the Ni/CGO co-impregnated LSCT$_{A-}$ anode before the first redox cycle, b) the Ni/CGO co-impregnated LSCT$_{A-}$ anode after the first redox cycle, c) the Ni/CeO$_2$ co-impregnated LSCT$_{A-}$ anode before the first redox cycle and d) the Ni/CeO$_2$ co-impregnated LSCT$_{A-}$ anode after the first redox cycle.

the first redox cycle, whilst figures 3c and d present the corresponding data for the Ni/CeO$_2$ cell.

Previous work on a variety of metal/CGO co-impregnated LSCT$_{A-}$ anode systems highlighted the fact that three distinct processes were observable within the AC impedance response of the SOFC at 850 °C: i) a high-frequency anode-related process (f_{max} = 700-250 Hz), denoted here as R$_{p1}$, ii) a mid-frequency cathode-related process (f_{max} = 20 Hz), denoted R$_{p2}$, and iii) a low-frequency gas conversion process (f_{max} = 2-3 Hz), denoted R$_{p3}$. [21,24] Figures 3a and b show that each of these processes can also be identified for the Ni/CGO cell tested here, in addition, to a higher-frequency process with a f_{max} of ~13 kHz, denoted R$_{p0}$ (for facile comparison to previous research). Given that a cathode response is not expected within this frequency domain, as shown in previous work, [24] this process most likely relates to the anode. [22]

In both complex plane plots, the current dependence of the R$_{p3}$ process can be clearly observed, further confirming that this arc relates to gas conversion; a process associated with gas composition, gas flow rate and test setup geometry. [28] As the current density drawn from the SOFC increases, more H$_2$ is oxidised to H$_2$O, increasing the p(H$_2$O) in the anode compartment and, thus, changing the equilibrium gas composition; directly reducing the resistance of the R$_{p3}$ process. Furthermore, in the Ni/CGO cell, although the R$_{p2}$ and R$_{p3}$ processes exhibit very similar f_{max} values to those identified previously, the R$_{p1}$ anode process exhibits a higher f_{max} of ~1 kHz. This is most likely due to the difference in test setups used at St Andrews (previous work) [24] and HEXIS test setups (this

work). For example, the flow rate of H$_2$ to the anode and the improved degree of separation of the air and fuel compartments, in the HEXIS test setups, most likely leads to a lower p(O$_2$) in the anode compartment. Before the redox cycling treatment, the R$_{p1}$, R$_{p2}$ and R$_{p3}$ processes can clearly be seen, with the R$_{p1}$ process dominating the impedance response. The R$_{p1}$ process is believed to correspond to the oxidation of H$_2$ that occurs at the triple phase boundary (TPB) between the Ni particle, the oxide-conducting ceria-component and the gas phase. However, as a result of this, the R$_{p0}$ process is largely masked and appears only to elongate the R$_{p1}$ arc in the high frequency region. After the first redox cycle was carried out, the R$_{p1}$ arc changes substantially. The f_{max} shifts from 1064 Hz to 847 Hz, allowing slightly improved resolution of the R$_{p0}$ process (which has a very small polarisation resistance), at the expense of the R$_{p2}$ process, which is almost completely masked by the increased polarisation resistance of the R$_{p1}$ anode process. This increase in resistance may relate to the loss of TPB length available for electrochemical oxidation of H$_2$, caused by agglomeration of Ni during redox cycling. Despite this rearrangement of the polarisation processes, the ohmic resistance (R$_s$) decreases; a commonly-observed phenomenon for these anodes, due the improvement in contacting between the anode surface and the Ni current collection paste. This, therefore, results in an improvement in area specific resistance (ASR) of 0.03 Ω cm^2.

The analogous spectra for the Ni/CeO$_2$ cell (figures 3c and d) show a similar behaviour before and after redox cycling, to the Ni/CGO cell. For example, before redox cycling, an asymmetric
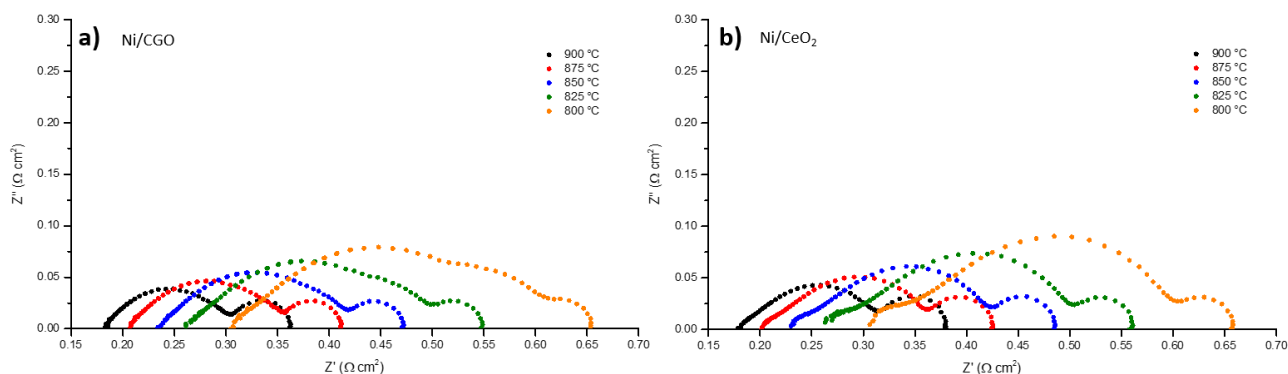
Figure 4. Complex plane AC impedance spectra collected at 300 mA cm^{-2} as a function of temperature for the SOFC containing: a) the Ni/CGO co-impregnated LSCT$_{A-}$ anode and b) the Ni/CeO$_2$ co-impregnated LSCT$_{A-}$ anode.

amalgam of the R$_{p0}$ and R$_{p1}$ processes can be identified, though it is much more difficult to separate the responses of these two processes, in this case. In addition, it is not possible to isolate the cathode contribution as the R$_{p1}$ process is so dominant, even before redox cycling has been performed. The ever-present gas conversion arc is well resolved and shows the same current-dependence as previously described. Interestingly, the redox cycle results in a much larger decrease in f$_{max}$ of the R$_{p1}$ process, from 1064 Hz to 428 Hz, implying that agglomeration of Ni may be more severe in the Ni/CeO$_2$ catalyst system than in the Ni/CGO catalyst system. However, as a result of this shift, excellent resolution of the R$_{p0}$ process is observed, further confirming that this process provides a very small contribution to the total polarisation resistance. It is tentatively suggested that this anode process may relate to transfer of oxide anions at the interface between the LSCT$_{A-}$ anode 'backbone' and the ceria-based coatings. Attempts have previously been made to deconvolve the high-frequency AC impedance spectra by altering the anode material employed within these SOFC and observing the resultant change. [22] Clear changes in this frequency domain were noted, however, the processes that arose were substantially more resistive and, therefore, masked the relatively small arc that was under investigation. [22] Thus, additional and more complex analysis of these AC impedance spectra is required to confirm this assumption. In contrast to the Ni/CGO cell, the redox cycle actually causes a degradation in the R$_s$ of the Ni/CeO$_2$ cell and, therefore, the ASR (0.04 Ω cm^2), potentially indicating a worsening of the nature of the contacting between the Ni current collecting paste and this particular anode microstructure.

In order to further confirm the identity of the previously assigned processes, AC impedance spectra were collected at 300 mA cm^{-2}, as a function of temperature. Figures 4a and b

illustrate the resultant spectra for the Ni/CGO cell and Ni/CeO$_2$ cell, respectively. The spectra for the Ni/CGO cell indicate that all processes are thermally activated, except for the R$_{p3}$ process, and fall into the previously reported frequency domains for the anode and cathode related processes. [24] The temperature independent nature of the R$_{p3}$ process confirms that this process does pertain to gas conversion impedance, which agrees well with previous work. [24] The R$_{p2}$ cathode arc is almost indiscernible at 900 °C, due to the dominance of the R$_{p1}$ process, however, the cathode response grows with decreasing temperature, dominating the low-frequency spectrum collected at 800 °C. Whilst the cathode limits performance to a certain extent, at lower temperatures, the anode R$_{p1}$ process is still the primary limiting factor at 800 °C, contributing 0.17 Ω cm^2 towards the ASR of 0.66 Ω cm^2. In addition, the R$_{p0}$ arc increases in resistance, though its contribution at 800 °C is only 0.04 Ω cm^2. The thermal activation of this process implies that it relates to an electrode process, most likely an anode related charge transfer process, as previously described.

The spectra for the Ni/CeO$_2$ cell (figure 4b) show the same trends in thermal activation (figure S1), however, the R$_{p2}$ process is almost entirely masked by the R$_{p1}$ process. Also, due to the fact that the R$_{p1}$ process occupies a slightly lower frequency domain, than for the Ni/CGO cell, better resolution of the high-frequency R$_{p0}$ process is observed, confirming that the resistance and temperature dependence of this process are similar for both SOFC. This provides further evidence that the R$_{p0}$ anode process is not governed by the electrochemical reactions that take place between the Ni particles and the ceria-based component but may represent a charge transfer process at another interface within the anode.

Additionally, a summary of the resistance values (table S2) obtained through equivalent circuit fitting of these temperature sweep AC impedance spectra (using the equivalent circuit models presented in figure 5) may be found in the accompanying supplementary information file, along with Arrhenius plots (figure S1) and activation energies (E$_a$) derived for R$_s$, R$_{p1}$, R$_{p2}$ and R$_{p3}$ (table S3). Calculation of the E$_a$ for R$_{p0}$ was omitted due to the influence of the R$_{p1}$ process on the comparatively small R$_{p0}$ process, especially at lower temperatures. For both Ni-containing cells, the R$_{p1}$ anode charge transfer processes exhibit a very similar E$_a$ (1.05 eV and
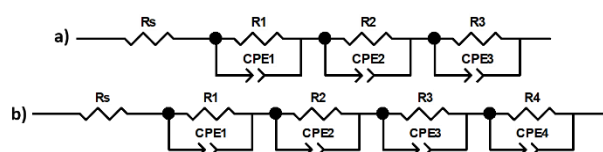

Figure 5. Equivalent circuit models used to fit experimental AC impedance spectra containing: a) three parallel resistor-constant phase element (R-CPE) units and b) four parallel R-CPE units.
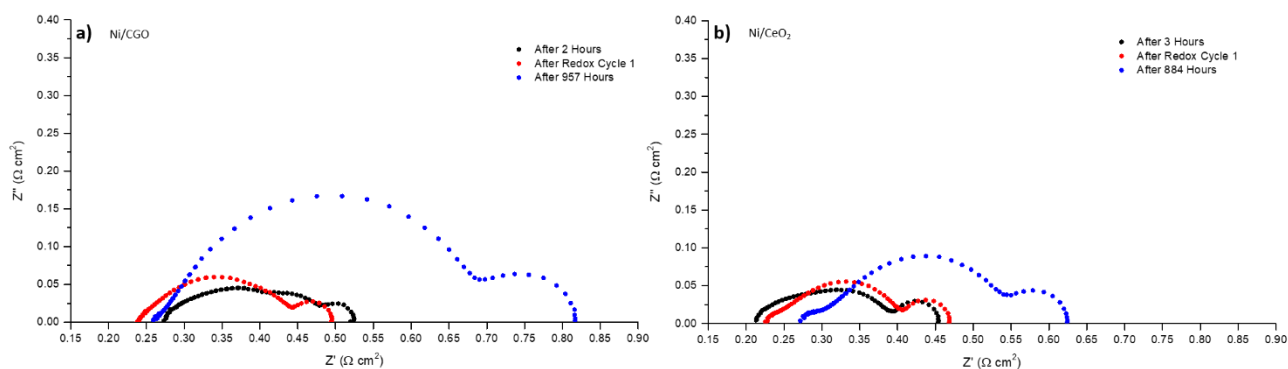
PAPER

Figure 6. Complex plane AC impedance spectra illustrating the temporal evolution of ohmic and polarisation resistances for: a) the SOFC containing the Ni/CGO co-impregnated LSCT$_{A-}$ anode and b) the SOFC containing the Ni/CeO$_2$ co-impregnated LSCT$_{A-}$ anode.

0.89 eV, respectively), which is typical for the fuel oxidation process occurring within these co-impregnated LSCT$_{A-}$ anodes. [24] As expected, despite the minor differences in process magnitude between these cells, the gas conversion impedance responses are characterised by negligible and identical E_a values of 0.10 eV, whilst cathode-related processes show E_a values of 0.99-1.01 eV, associated with the reduction of adsorbed and dissociated oxygen at the TPB of the cathode. Finally, the activation energy pertaining to the series resistance of Ni/CGO and Ni/CeO$_2$ cells was 0.66 eV, for both cells. As the series resistance of SOFC should correspond solely to the ionic conductivity of the electrolyte, in theory, an activation energy of 0.78 eV would be expected for the 6ScSZ electrolyte in this temperature range. [29] The discrepancy between the experimental and theoretical E_a values highlighted here can be explained by additional ohmic contributions from the limited electronic conductivity LSCT$_{A-}$ anode 'backbone'. [16,24]

Temporal performance evolution of the Ni/CGO and Ni/CeO$_2$ cells. In order to determine the major causes of degradation within these two SOFC, three AC impedance spectra, collected at different stages of testing, were subjected to equivalent circuit fitting. The selected data were collected at 850 °C and 300 mA cm^{-2}: i) before the first redox cycle was performed, ii) after the first redox cycle was performed and iii) upon conclusion of the test period. Figures 5a and b show the equivalent circuit models used to analyse the AC impedance spectra, with three and four elements representing polarisation processes, respectively. Here, R_s represents the ohmic resistance of the SOFC, whilst the R-CPE unit represents a resistor connected in parallel to a constant phase element (used to model pseudocapacitive behaviour).

Figure 6a presents the relevant AC impedance spectra for the Ni/CGO cell, whilst accompanying equivalent circuit fitting parameters are included in table 1. As previously noted, the redox cycle benefits the SOFC in terms of the R_s, dropping from 0.27 Ω cm^2 to 0.24 Ω cm^2, however, the R_{p1} process actually increases in resistance slightly (0.09 Ω cm^2 to 0.10 Ω cm^2) and the corresponding f_{max} drops reduces to 847 Hz from 1340 Hz. This is consistent with agglomeration of Ni, and loss of TPB length at the interface between the Ni and CGO components, which is known to occur due to the redox instability of Ni. Also, despite a slight improvement in the polarisation resistance of the R_{p0} process, the R_{p2} and R_{p3} processes remain unaffected, as expected, due to the stability of the cathode materials and the constant nature of the test conditions that give rise to gas conversion. Considering the spectrum collected after 957 hours of operation, the R_{p1} process dominates the entire high to mid-frequency region of the spectrum. The shift in f_{max} of this process from 847 Hz to 137 Hz, coupled with the 200 % increase in polarisation resistance of this anode charge transfer process, in comparison to the value extracted from the spectrum collected after the first redox cycle, indicates that agglomeration of Ni continues throughout the operational period and contributes the most towards degradation. Degradation of the R_s and R_{p0} process is relatively minor in comparison, whilst the R_{p2} process remains constant, despite being heavily masked by the dominant R_{p1} process, which is expected as cathode process should not degrade significantly over this time period. Surprisingly, though, at the low-frequency end of this spectrum, a substantially more resistive process appears, which occupies the same frequency domain as the gas conversion process. Initially, the theory that severe agglomeration of Ni nanoparticles caused changes in the nanostructure, and thus the flow pathways throughout the anode, was considered as an explanation for increasing the polarisation resistance of the gas conversion process. However, an almost three-fold increase in R_{p3} was deemed unlikely to

Table 1. A summary of the resistance values obtained from equivalent circuit fitting of the AC impedance spectra for the temporal evolution of the Ni/CGO and Ni CeO$_2$ cells.

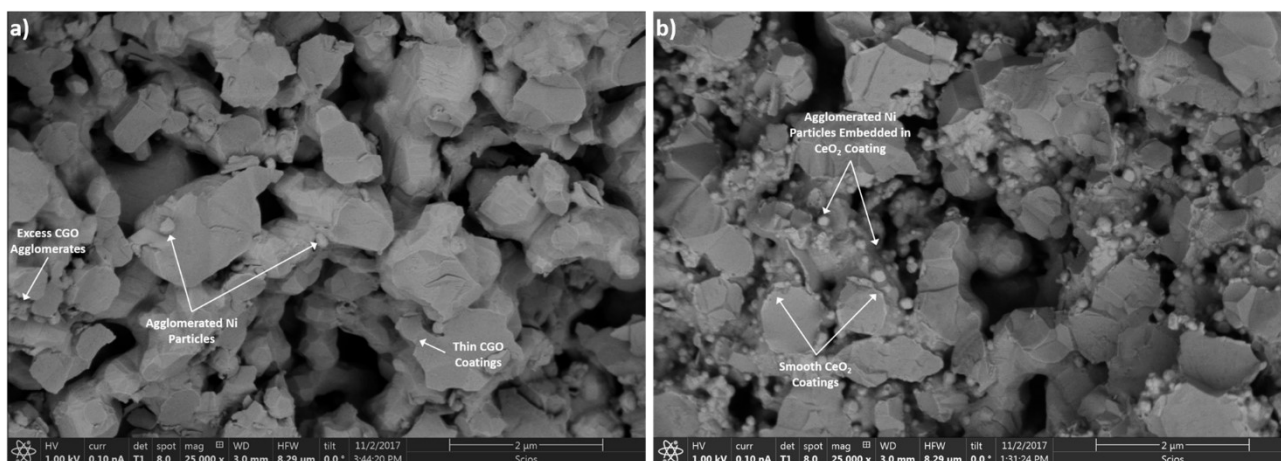|	Ni/CGO						Ni/CeO$_2$					
Spectrum	\multicolumn{6}{c}{Process Resistance/ Ω cm^2}	Spectrum	\multicolumn{6}{c}{Process Resistance/ Ω cm^2}
	R_s	R_{p0}	R_{p1}	R_{p2}	R_{p3}	R_{p4}		R_s	R_{p0}	R_{p1}	R_{p2}	R_{p3}	R_{p4}
2 Hours	0.27	0.05	0.09	0.07	0.05	-	3 Hours	0.21	0.06	0.07	0.06	0.06	-
Redox Cycle 1	0.24	0.04	0.10	0.07	0.05	-	Redox Cycle 1	0.22	0.05	0.08	0.06	0.06	-
957 Hours	0.26	0.06	0.30	0.07	-	0.13	884 Hours	0.27	0.06	0.16	0.06	-	0.08

Figure 7. Backscattered SEM images of the broken cross-sections of a) the Ni/CGO co-impregnated LSCT$_{A-}$ anode and b) the Ni/CeO$_2$ co-impregnated LSCT$_{A-}$ anode.

originate as a result of Ni agglomeration when considering that the gas conversion processes observed during short-term testing of these anodes at St Andrews [24] and durability testing at HEXIS (presented here) are nearly identical, in test setups that have notable differences in geometry and gas flow rate. An alternative explanation that may account for the appearance of this new low-frequency contribution (denoted R$_{p4}$) can be found in the literature concerning the effects of chemical capacitance (C$_{chem}$). As suggested by the name of this phenomenon, C$_{chem}$ is a purely or almost-purely capacitive process that arises due to the build-up of charge in the bulk of MIEC materials, e.g. CGO. [30–33] Under the low p(O$_2$) conditions of a SOFC anode compartment, in the case of CGO, a proportion of Ce^{4+} species would be reduced to Ce^{3+} species and oxygen vacancies would be created, leading to the accumulation of charge in the bulk of the phase. [30–35] Chueh et al. showed that a low-frequency arc in the AC impedance spectra of samaria-doped-ceria (SDC) thin films pertained to C$_{chem}$, giving rise to large capacitance values (1 − 100 F cm^{-2}) that could not originate from interfacial capacitances. [30] Moreover, Burnat et al. determined that a process occupying a similar frequency domain (1 − 0.1 Hz) in SOFC containing porous composite anodes of La$_{0.20}$Sr$_{0.70}$TiO$_3$-Ce$_{0.90}$Gd$_{0.10}$O$_{1.95}$ (LST-CGO), also related to C$_{chem}$. [31] In addition, they found that the shape and magnitude of this low-frequency process was influenced by the surface area of the MIEC component available in the microstructure, due to potentially limited reaction kinetics for the adsorption, oxidation and desorption of the fuel gas (H$_2$). [31] Therefore, it is feasible that any changes in the impregnated CGO component (or to a lesser extent, the MIEC LSCT$_{A-}$ component) employed in these co-impregnated LSCT$_{A-}$ anodes, pertain to C$_{chem}$ and may give rise to the low frequency process (2 Hz), which appears to completely mask the previously observed gas conversion process. Correlation of the development of this low-frequency AC impedance response to post-mortem microscopic analysis, provided in the following sections, highlights a potential pathway through which this may arise.

Capacitances for the R$_{p4}$ process, derived from the data in table 1, are 0.75 F cm^{-2} and 1.12 F cm^{-2} for the Ni/CGO and Ni/CeO$_2$ cells, respectively. It should also be noted that gas conversion impedances exhibit large capacitance values (e.g. 1 − 2 F cm^{-2}), as shown by Primdahl and Mogensen, [28,36] that are several orders of magnitude larger than interfacial capacitances. Therefore, the low-frequency response concerned here is likely to be an amalgam of both gas conversion and chemical capacitive processes. Practically, it is difficult to separate the resistive contributions of gas conversion and chemical capacitance in a 'sealless' system. Measurement and controlled variation of the p(O$_2$) in the anode chamber may well help to distinguish these contributions, however employment of a sealed system would be required, which may not result in AC impedance responses that are representative of (or relevant to) the inherently unsealed HEXIS system. Therefore, as only a single AC impedance spectrum from the end of the test period is available, without information about the effect of temperature, current density or p(O$_2$) on this process, this is a tentative assignment. A summary of the resistance and capacitance values for the R$_{p3}$ process (at the start of the test period) and R$_{p4}$ process (at the end of the test period) may be found in the accompanying supplementary information file (table S4) for each SOFC tested.

Figure 6b presents the analogous data for the Ni/CeO$_2$ cell, with accompanying equivalent circuit fitting data in table 1. In similarity to the Ni/CGO cell, the redox cycle results in an increase of polarisation resistance of the R$_{p1}$ process, strengthening the argument that this anode charge transfer process is dependent on the identity of the metallic catalyst component (in this case: Ni). Little change is observed in the other polarisation processes, however, the R$_s$ increases as a result of the redox cycle and, indeed, long term operation (after 884 hours) indicating that contacting between the Ni paste current collector and the anode surface was poor. However, between the spectra collected after the first redox cycle and 884 hours operation, R$_{p1}$ degrades by 100 % which is substantially lower than the analogous degradation observed for the Ni/CGO cell. Therefore, although the initial degradation exhibited by the Ni/CeO$_2$ impregnated LSCT$_{A-}$ anode is slightly larger than for the Ni/CGO cell, the rearrangement of the interface between the Ni catalyst and the CeO$_2$ coating results in a more stable anode nanostructure, than was achieved for
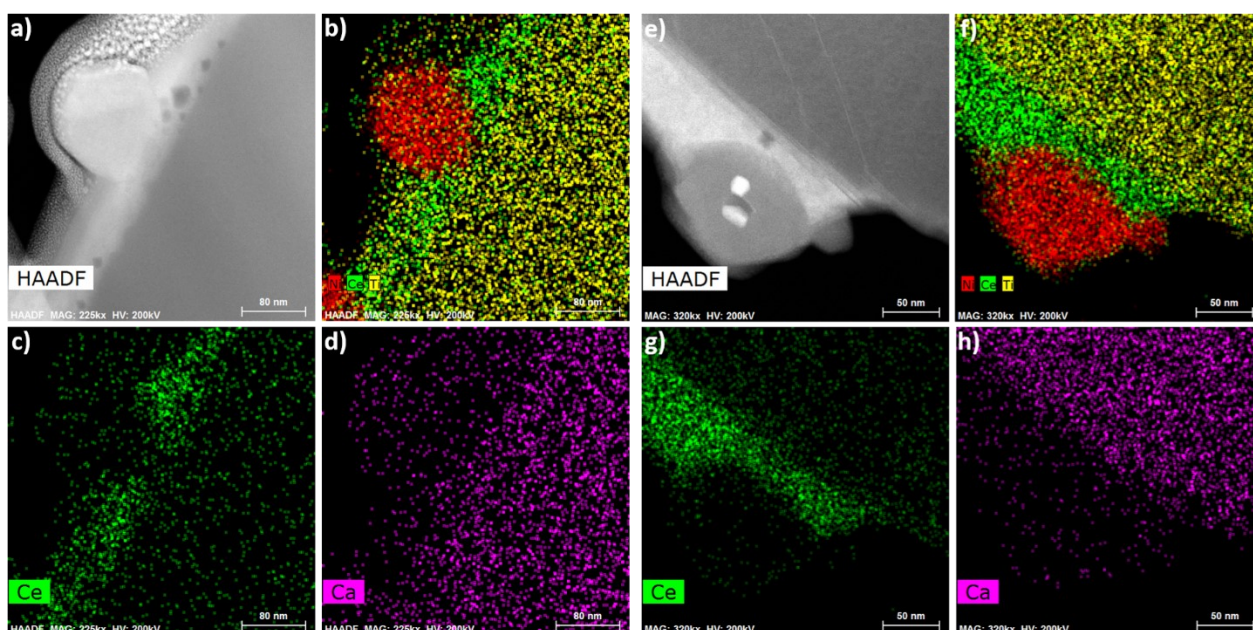
Figure 8. STEM images and accompanying EDX maps for regions of a-d) a FIB-milled cross-section of the Ni/CeO$_2$ co-impregnated LSCT$_{A-}$ anode and e-h) a FIB-milled cross-section of the Ni/CGO co-impregnated LSCT$_{A-}$ anode.

the Ni/CGO impregnated LSCT$_{A-}$ anode. Once again, this indicates that the interaction between the metallic catalyst component and the ceria-based catalyst component is crucial in determining the ultimate stability of performance achieved using this type of anode. Finally, considering the low-frequency process, an increase in polarisation resistance is observed for the Ni/CeO$_2$ cell, though this increase is not as large as that exhibited by the Ni/CGO cell. Once again, this process does not represent gas conversion, as this should remain constant throughout the test period, but it may pertain to C$_{chem}$.

Post-mortem microscopic analysis of the Ni/CGO and Ni/CeO$_2$ co-impregnated LSCT$_{A-}$ anodes. Post-mortem SEM was performed on fractured cross-sections of the SOFC, focussing on the Ni/CGO and Ni/CeO$_2$ impregnated LSCT$_{A-}$ anodes, in order to identify features that gave rise to differences in degradation rate. For the purposes of comparison, examples of the initial appearance of similar Ni-containing anodes, that have been exposed to reducing conditions for approximately 5 hours during SOFC testing, are presented elsewhere. [24,37] Figure 7a shows a back-scattered electron (BSE) micrograph of a region of the Ni/CGO impregnated LSCT$_{A-}$ anode. It is clear that the nanostructure of the anode has largely been destroyed and very few Ni particles remain, exhibiting an average diameter of 192 nm. Strikingly, the oxide-ion conducting CGO component does not appear to coat the LSCT$_{A-}$ anode 'backbone' microstructure evenly. In some areas, very thin coatings can be seen, with other areas containing irregularly shaped islands and even
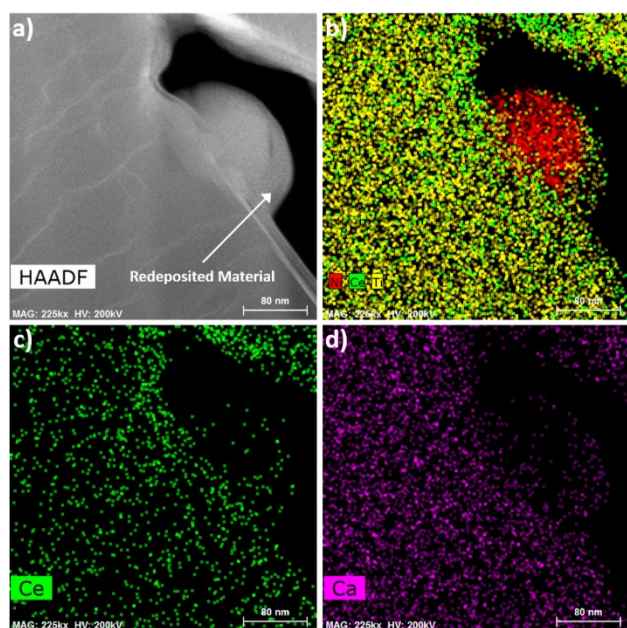

Figure 9. STEM image (a) and accompanying EDX maps (b-d) for a region of the Ni/CGO co-impregnated LSCT$_{A-}$ anode showing an agglomerated Ni particle resting on a very thin layer of CGO.
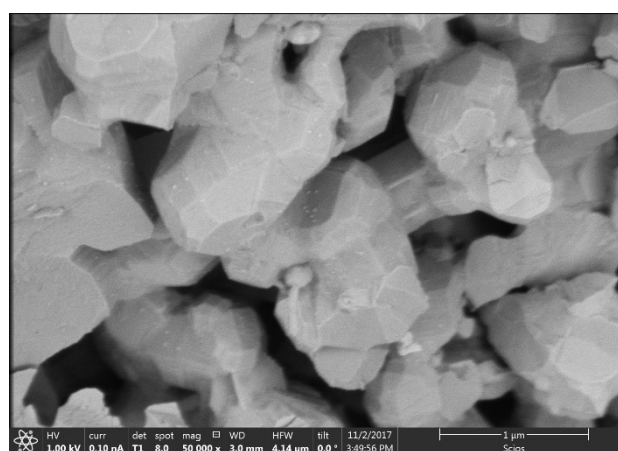

Figure 10. Backscattered SEM image of a broken cross-section of the Ni/CGO co-impregnated anode showing a region that has retained few Ni nanoparticles after testing.

agglomerates of CGO in the pores (indicated in figure 7a). As previously noted for this system type, the metallic catalyst component preferentially locates on to the ceria-based component. [16,24] Therefore, as the majority of the LSCT$_{A-}$ 'backbone' appears to be bare of CGO, there are very few areas in which Ni particles are able to sit upon the impregnated CGO layers for improved anchorage and stability. As a result, this lack of stability has incited agglomeration of nanoscale Ni particles into large agglomerates, [16,38,39] reducing the catalytically active surface area and, thus, the TPB length available for H$_2$ oxidation. Additionally, an important role of the CGO catalyst component is to provide high ionic conductivity to these anode microstructures, therefore, a further significant consequence of agglomeration of this catalyst phase is the disruption of oxide-ion conduction pathways within the anode. In comparison, the BSE micrograph presented for the Ni/CeO$_2$ impregnated LSCT$_{A-}$ anode (figure 7b) shows that the majority of the LSCT$_{A-}$ anode microstructure is coated in a layer of the CeO$_2$ catalyst component (indicated in figure 7b). Consequently, the angular, terraced LSCT$_{A-}$ grain surfaces can no longer be seen, but instead a smooth CeO$_2$ coating, harbouring a high population density of Ni catalyst particles, is present. The fact that there are so many Ni particles (with an average diameter of 131 nm) still preferentially located on the CeO$_2$ layer indicates that CeO$_2$ provides greater stabilising effect to Ni than CGO does over the test period of ~1000 hours. Furthermore, examination of FIB-milled cross-sections of both anodes, using STEM and EDX mapping, revealed that Ni particles within the Ni/CeO$_2$ impregnated anode were typically embedded within laterally continuous CeO$_2$ coatings (with a thickness of 51 nm to 71 nm), upon the LSCT$_{A-}$ 'backbone' (figures 8a to d), whilst Ni particles within the Ni/CGO impregnated anode were either embedded in isolated 'islands' of CGO (figures 8e to h) or were almost resting directly upon the LSCT$_{A-}$ anode 'backbone', save for a very thin layer of CGO beneath the Ni particle (figures 9a to d).

Also, in figure 8e it is possible to identify some Au nanoparticles resting upon the surface of the FIB-milled cross-section of the Ni particle. The origin of these Au particles is unknown, as Au paste current collectors were not employed on the anode side (only Au mesh on the cathode side), however, as they rest upon the surface of the cross-section rather than being embedded within the core of the Ni nanoparticle, they were
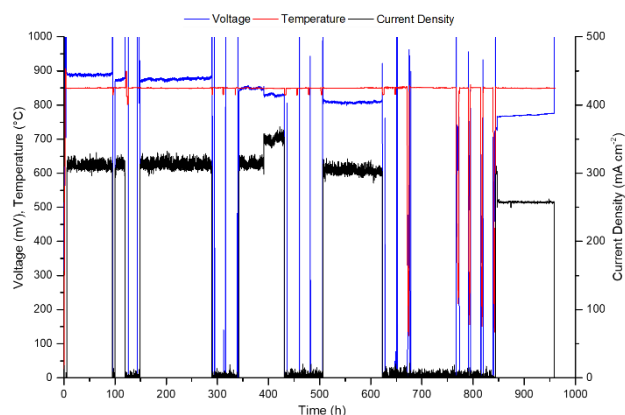

Figure 11. Long-term galvanostatic operation of the SOFC containing a Pt/CGO co-impregnated LSCT$_{A-}$ anode, including redox, thermo and thermoredox cycling treatments.

most likely inadvertently deposited during preparation of the cross-section. Regardless of this, Au is known to be 'inert' in the atmospheric conditions of the anode chamber, hence its common use as a current collector for anodes, therefore its presence would not be expected to affect performance, even if the Au nanoparticles were present in the anode nanostructure during testing.

Despite the severe agglomeration of Ni particles in both the Ni/CGO and Ni/CeO$_2$ impregnated LSCT$_{A-}$ anode systems, the absence of Ni particles in the former system is undoubtedly the reason why it degraded almost twice as much (in terms of voltage) as the latter. This is ultimately controlled by the distribution, morphology and wettability of the ceria-based component upon the LSCT$_{A-}$, and the subsequent affinity of the metallic catalyst to preferentially locate onto the ceria-based component. In addition, though, the interfacial energy [40] that arises between the metallic catalyst component (i.e. Ni in these systems) and the ceria-based component is crucial in determining the extent of embedding or anchorage of the Ni catalyst phase, which is widely-reported to be highly mobile under reducing conditions. [41,42] In very few areas of the Ni/CGO impregnated LSCT$_{A-}$ anode, for example, very fine Ni nanoparticles (16 nm average diameter) can be identified upon the LSCT$_{A-}$ 'backbone', in the form that they are expected to be deposited after impregnation (figure 10). However, after only
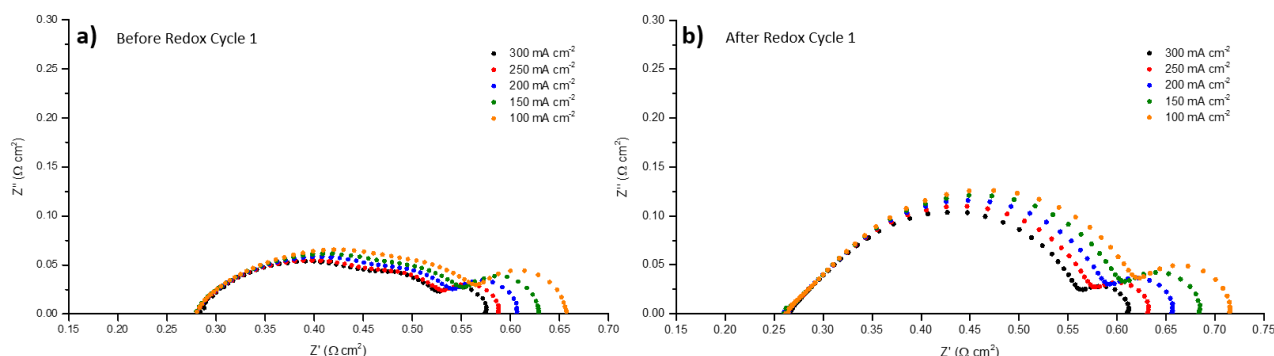

Figure 12. Complex plane AC impedance spectra collected at 850 °C as a function of current density for the SOFC containing the Pt/CGO co-impregnated LSCT$_{A-}$ anode: a) before the first redox cycle and b) after the first redox cycle.
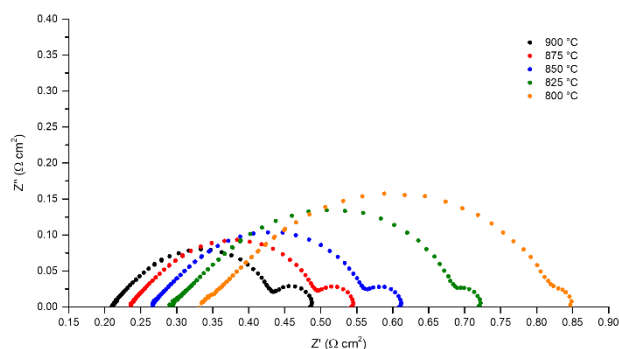
Figure 13. Complex plane AC impedance spectra collected at 300 mA cm^{-2} as a function of temperature for the SOFC containing the Pt/CGO co-impregnated LSCT$_{A-}$ anode.
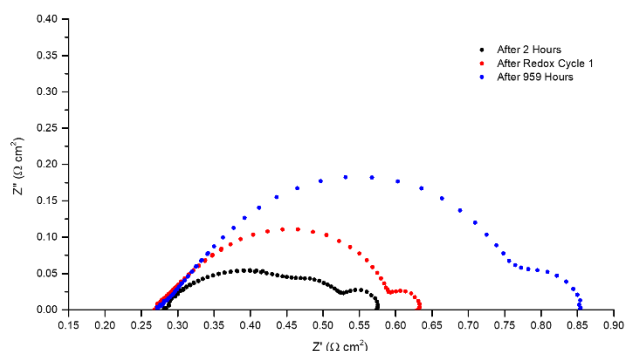

Figure 14. Complex plane AC impedance spectra illustrating the temporal evolution of ohmic and polarisation resistances for the SOFC containing the Pt/CGO co-impregnated LSCT$_{A-}$ anode.

1000 hours of operation the size increases by an order of magnitude, highlighting the severe tendency of Ni to move and agglomerate during operation.

Correlating these observations to the changes in performance displayed by the AC impedance spectra in figure 6 provides information on two interlinked sources of degradation in these anodes.

Firstly, the severe agglomeration of the impregnated Ni phase in both the Ni/CGO and Ni/CeO$_2$ cells and loss of TPB length between the gas phase, Ni particles and ceria-based component, couples well with the increase in the resistance of the R$_{p1}$ anode-related process. The poorer wettability (and stability) of CGO upon the LSCT$_{A-}$ 'backbone', in comparison to the CeO$_2$ component, leads to more severe agglomeration of the CGO component, reducing the area of CGO available for Ni to rest upon. Therefore, the lack of 'stabilising' CGO surface area further incites the agglomeration of Ni, giving rise to almost double the degradation in comparison to the Ni/CeO$_2$ cell.

Secondly, the agglomeration of CGO has an additional effect on the form of the impedance spectra obtained. As discussed by Burnat *et al.*, the C$_{chem}$ process observed at low frequency (2 Hz in this work) scales inversely with surface area of ceria-based component available for adsorptive, desorptive and oxidative processes of the fuel gas. [31] Therefore, the severe agglomeration of the CGO component, the reduction of its surface area and the disruption of the percolating oxide-ion conducting network it forms, most likely gives rise to the R$_{p4}$ process which completely masks gas conversion after 957 hours of operation. In comparison, from STEM and EDX analysis, the CeO$_2$ component in the Ni/CeO$_2$ cell remains upon the backbone and has agglomerated to a lesser extent, thus the C$_{chem}$ process (R$_{p4}$) is much less resistive than for the Ni/CGO cell.

Characterisation of the Pt/CGO co-impregnated LSCT$_{A-}$ anode

Long-term galvanostatic operation of the Pt/CGO cell. The long-term measurement data obtained under galvanostatic operation for the SOFC containing a LSCT$_{A-}$ anode, impregnated with 13 wt. % CGO and 2 wt. % Pt (Pt/CGO cell), is presented in figure 11. In similarity to the test conditions of the Ni/CGO cell, there is instability in the current density extracted from the SOFC due to issues with the current sink employed for testing. The total voltage degradation exhibited by the Pt/CGO cell was 13.4 % (270 mΩ cm^2 in terms of ASR) over the 959 hour test period, showing great similarity to the degradation characteristics of the Ni/CGO cell (14.9 % or 290 mΩ cm^2 in terms of ASR). However, between approximately 92 hours and 343 hours, both the Ni/CGO and Pt/CGO cells were exposed to 4 redox cycles. The resultant degradations observed were 22 mV and 45 mV, respectively, indicating that, initially, the redox stability of the Pt/CGO cell was lower than that of the Ni/CGO cell. Despite the severity of this initial degradation in performance, the degradation in operating voltage and ASR stabilises during operation at 300 mA cm^{-2} (506 hours to 623 hours) and, even after the intense period of redox/thermo/thermoredox cycling executed between 623 hours and 847 hours, the SOFC operating voltage remains stable and even recovers slightly under galvanostatic operation.
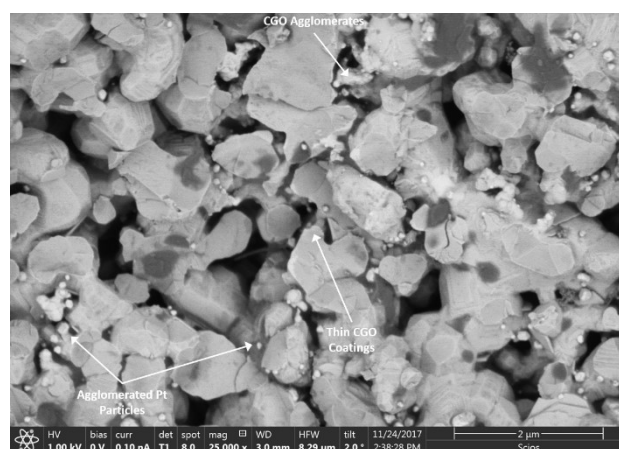
Table 2. A summary of the resistance values obtained from equivalent circuit fitting of the AC impedance spectra for the temporal evolution of the Pt/CGO cell.

Spectrum	Process Resistance/ Ω cm^2					
	R$_s$	R$_{p0}$	R$_{p1}$	R$_{p2}$	R$_{p3}$	R$_{p4}$
2 Hours	0.28	0.06	0.11	0.08	0.05	-
Redox Cycle 1	0.27	0.06	0.18	0.07	0.05	-
959 Hours	0.27	0.06	0.36	0.06	-	0.10

Figure 15. Backscattered SEM image of the broken cross-section of the Pt/CGO co-impregnated LSCT$_{A-}$ anode.

Overall, this indicates that the Pt metallic catalyst offers improved redox stability over the Ni metallic catalyst, when co-impregnated with CGO. In reality, though, the 13.4 % voltage degradation is still unacceptable for long-term operation in a SOFC.

AC impedance spectroscopic analysis of the Pt/CGO cell. AC impedance spectroscopy was used to characterise the performance of the Pt/CGO cell as a function of current density and temperature. Firstly, spectra were collected at 850 °C and current densities between 100 and 300 mA cm^{-2}, before and after the first redox cycle was performed (Figure 12a and 12b, respectively). In figure 12a, it is possible to see that 3 distinct processes are present: i) a high-frequency anode charge-transfer process (R_{p1}), a mid-frequency cathode charge-transfer process (R_{p2}) [24,43] and a low-frequency gas conversion process (R_{p3}). [24,28] As expected, the R_{p2} and R_{p3} processes are very similar to those identified for the Ni/CGO and Ni/CeO$_2$ cells, which is rational given the use of the same cathode and the test setup/parameters across all of these tests. Furthermore, the shape of the R_{p1} arc is remarkably similar for the Ni/CGO and Pt/CGO cells. The higher-frequency process (R_{p0}) is also present in this spectrum, though it is heavily masked by the dominant R_{p1} process. Nevertheless, the dominant anode charge transfer (R_{p1}) process is activated by increasing current density, as is the gas conversion process, due to the increased $p(H_2O)$ that arises from increased H$_2$ oxidation at higher current densities. The cathode charge transfer process shows minimal change in resistance as a function of current density, though it appears to be heavily influenced by the resistance and frequency domain of the R_{p1} process.

Examining figure 12b, it is possible to see that the redox cycle has a significant impact on the shape of the spectra and, consequently, the ASR of the SOFC. The resistance of the R_{p1} arc increased, whilst the f$_{max}$ of the process shifted to a lower frequency domain, completely masking the R_{p2} cathode charge transfer arc. As a direct result, the resolution of the R_{p0} arc improves and the gas conversion process can still be easily identified at the low-frequency end of the spectrum. As described for the pre-redox cycle spectra, each process behaves in a very similar manner, when the current density is increased.

Figure 13 shows the AC impedance spectra for the Pt/CGO cell collected at 300 mA cm^{-2} as a function of temperature. Unfortunately, due to the increased polarisation resistance of the R_{p1} process, caused by the redox cycle, it is very difficult to identify additional processes within these temperature sweep spectra, especially since the thermal activation of this process is so large. Although R_{p2} is known to grow with decreasing temperature and become particularly dominant at 800 °C, as previously reported, [24] it is the anode charge transfer process that is rate limiting at all temperatures for this Pt-containing SOFC. The first redox cycle is thought to cause severe agglomeration of the Pt catalyst particles and nanoparticles, in similarity to the behaviour of Ni nanoparticles, reducing the specific surface area available for oxidation of H$_2$ and increasing the polarisation resistance pertaining to anode charge transfer. Moreover, the process resistances from equivalent circuit

fitting of the Pt/CGO cell temperature sweep AC impedance data (table S2) and accompanying Arrhenius plots (figure S1) may be found in the supplementary information file. The activation energies (table S3) determined for R$_s$, R$_{p2}$ and R$_{p3}$ processes show great similarity to those identified for the Ni-containing cells, due to the employment of the same electrolyte, cathode and test setup. Furthermore, the Pt/CGO cell exhibits a slightly lower E$_a$ (0.97 eV), in comparison to the Ni/CGO cell, for the anode-related R$_{p1}$ process, however, this still falls within the realm of charge transfer during fuel oxidation, as expected.

Temporal performance evolution of the Pt/CGO cell. In order to determine which processes gave rise to the 13.4 % voltage degradation throughout the operational period, a temporal evolution of AC impedance spectra is presented in figure 14. These spectra were subjected to equivalent circuit fitting using the circuits shown in figure 5 and accompanying fitting parameters have been included in table 2.

The spectra collected before and after the first redox cycle indicate that a 0.01 Ω cm^2 reduction in R$_s$ is achieved, which is typically caused by improved contacting between the Ni current collector and anode surface. Furthermore, as previously noted, the shape of the spectrum changes drastically after the first redox cycle was performed. Here, the increase in polarisation resistance of the anode charge transfer process, by 64 %, causes masking of the cathode charge transfer process. This increase in resistance, following a redox cycle, is associated with the agglomeration of the metallic catalyst component, reducing the length of the triple phase boundary, between the CGO and Pt components, available for H$_2$ oxidation. After 959 hours of operation, the R$_s$ showed very little degradation, indicating that contacting of the electrodes by the current collectors had not worsened and that the optimised microstructure of the LSCT$_{A-}$ 'backbone' was sufficient to prevent poor current distribution and localised degradation within the anode or delamination at the anode/electrolyte interface. As expected, the resistive contribution from the R$_{p1}$ process increased further as a function of operation (and agglomeration of Pt particles), giving a final polarisation resistance of 0.36 Ω cm^2. As observed for the Ni/CGO cell, the gas conversion process is masked by the aforementioned C$_{chem}$ process (C = 0.60 F cm^{-2}), whose resistance grows as a function of operating temperature and agglomeration of the CGO component.

Post-mortem microscopic analysis of the Pt/CGO anode. Figure 15 shows a backscattered electron micrograph of a broken cross section of the tested Pt/CGO anode. In this microstructure, it is possible to see that a relatively small number of agglomerated Pt particles remains, however, the CGO coatings appear to have broken up and no longer act as an 'anchoring' layer between the LSCT$_{A-}$ 'backbone' and the Pt particles. The lack of stability offered to the Pt particles in this anode is, therefore, the major cause of degradation in operating voltage and internal resistance, which aligns well with the interpretations drawn from the AC impedance analysis. This conclusion is further corroborated by the micrographs and EDX maps, collected using
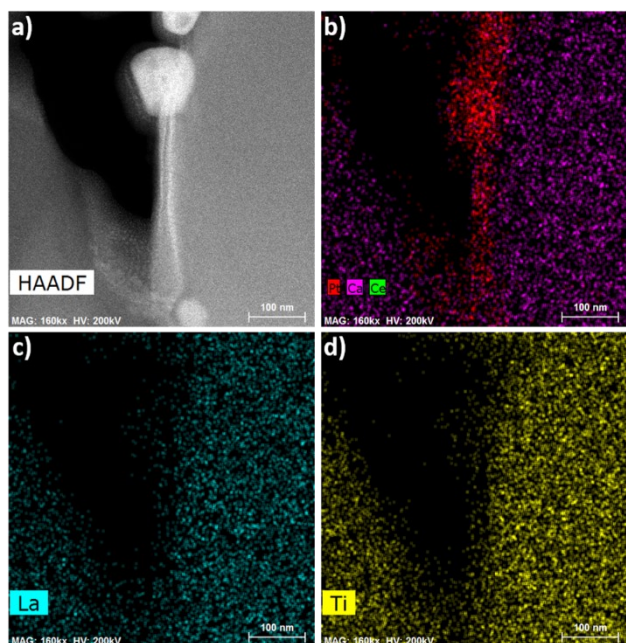
Figure 16. STEM image (a) and accompanying EDX maps (b-d) for a region of a FIB-milled cross-section of the Pt/CGO co-impregnated LSCT$_{A-}$ anode.

STEM, presented in figures 16 and 17. In both of these micrographs, it is possible to identify Pt particles (which have agglomerated to between 49 nm and 115 nm) resting directly upon the LSCT$_{A-}$ anode microstructure, without a CGO coating present to stabilise this metallic catalyst phase, giving rise to the increase in R$_{p1}$. The agglomerated CGO particles illustrated in figure 15 and the lack of CGO coated LSCT$_{A-}$ grains shown in figures 16 and 17 further reinforce the theory that the R$_{p4}$ process grows as a function of operational time, dominating the low-frequency AC impedance spectrum after 959 hours of operation. In figure 16b, the vertically extensive signal
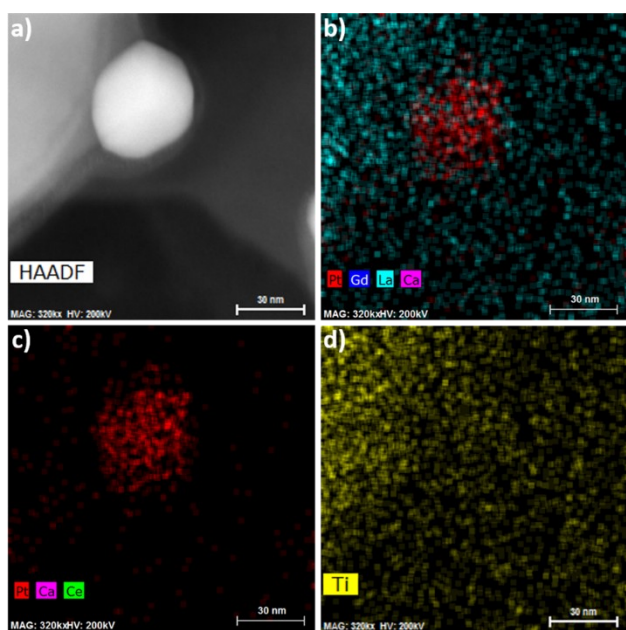

Figure 17. STEM image (a) and accompanying EDX maps (b-d) for a region of a FIB-milled cross-section of the Pt/CGO co-impregnated LSCT$_{A-}$ anode.

pertaining to Pt indicates the presence of a protective layer of Pt (and C), deposited to protect the surface features during FIB-SEM preparation of this sample, whilst Pt catalyst particles appear as spherical particles within this EDX map. Ultimately, the mechanism of degradation observed in this anode catalyst system is identical to those observed in the Ni/CGO cell, though the Pt catalyst phase appears to be marginally more stable over similar periods of operation in realistic SOFC testing conditions. Moreover, this reinforces the fact that it is not only the ability of the specific composition of ceria-based component which gives rise to improved/worsened stability of metallic catalyst particles, but rather the interaction and mutualistic relationship between the particular metallic catalyst and ceria-based component, as shown by the stability of SOFC containing Rh/CGO co-impregnated LSCT$_{A-}$ anodes at button cell and short stack scales. [25]

Conclusions

Electrolyte-supported SOFC containing Ni/CGO, Ni/CeO$_2$ and Pt/CGO impregnated LSCT$_{A-}$ anodes were tested in industrial test setups for ~1000 hours at HEXIS. All SOFC, operated at 850 °C and 300 mA cm^{-2}, showed relatively low degradation as a result of redox cycling, however, the voltage degradation associated with these treatments was lower for the Ni/CeO$_2$ impregnated anode than the Ni/CGO and Pt/CGO impregnated anodes.

Considering the Ni-containing anodes, thermo and thermoredox cycling treatments caused failure of the Ni/CGO impregnated anode, whilst the performance of the Ni/CeO$_2$ impregnated anode remained stable during and after cycling. Ultimately, the voltage degradation observed for the SOFC with the Ni/CGO impregnated anode (14.9 %) was almost double that exhibited by the SOFC with the Ni/CeO$_2$ impregnated anode (7.7 %). This difference is attributed to the composition of the ceria-based component employed in each anode and the resultant stabilising interaction between this component and the Ni catalyst particles. Post-mortem microscopic analysis revealed that CeO$_2$ coated the LSCT$_{A-}$ anode 'backbone' microstructure uniformly and a large population of Ni particles (~100 nm diameter) remained embedded in this coating, within the microstructure. In contrast, the CGO component, in the Ni/CGO impregnated anode, formed irregular 'islands' upon the LSCT$_{A-}$ 'backbone' and agglomerates in microstructural pores. As a result, fewer suitable (typically flat) areas of the ceria-based component were available for Ni particles to locate upon, resulting in poorer anchorage and stability of the Ni particles. This ultimately explains the low numbers of highly agglomerated Ni particles that remained within the anode after testing and the accompanying degradation in performance for the SOFC containing the Ni/CGO impregnated anode. Significantly, though, the agglomeration of the CGO component also led to the development of an additional low-frequency process, observed toward the end of the operational period that totally masked the gas conversion process. This is tentatively attributed to chemical capacitance, which arises due to the accumulation of charge in the bulk of MIEC materials,

such as CGO, and is coupled with kinetic limitations of fuel adsorption, desorption and oxidation at the available surface area of this impregnated ceria-based component.

In contrast, the SOFC containing the Pt/CGO impregnated anode exhibited a substantial increase in the anode polarisation resistance over the course of the first 4 redox cycles, indicating that the Pt catalyst particles had agglomerated severely. Thermo and thermoredox cycling resulted in comparatively small voltage degradation, however, performance stabilised after the final thermoredox cycle was executed and the operating voltage even recovered slightly during galvanostatic operation over the final ~100 hours of the test period. SEM and STEM imaging, with accompanying EDX analysis, confirmed that the Pt catalyst particles had agglomerated (up to 115 nm in diameter) and the CGO coatings (on the LSCT$_{A-}$ grains) had migrated/agglomerated and could not be easily identified (further increasing the tendency for Pt particles to agglomerate and increasing the chemical capacitive response of MIEC CGO phase). Ultimately, this led to a similar total voltage degradation as the SOFC containing the Ni/CGO impregnated anode: 13.4 % over the full 959 hour operational period.

Systematic variation of both the metallic catalyst and ceria-based catalyst phases within these co-impregnated, nanostructured LSCT$_{A-}$ anodes has, therefore, highlighted two key aspects which must be carefully controlled in order to minimise degradation. Firstly, a metallic catalyst component that exhibits high electrocatalytic activity for fuel oxidation and a low propensity to agglomerate with other like particles should be chosen. Secondly, and most importantly, a composition of ceria which provides continual anchorage to that specific metallic catalyst throughout the operational period must be chosen. This means that the ceria-based component must resist agglomeration to provide a continuous coating or series of 'islands' onto which the metallic catalyst particles can locate and be stabilised against their own mechanisms of agglomeration. Should this ceria-based layer disperse or migrate, severe voltage degradation is likely to ensue due to consequent accelerated metallic catalyst agglomeration and due to the gradual development of low-frequency chemical capacitive effects.

Conflicts of interest

There are no conflicts to declare.

Acknowledgements

References

1   S. Singhal, *Solid State Ionics*, 2000, **135**, 305–313.
2   N. Q. Minh, *J. Am. Ceram. Soc.*, 1993, **76**, 563–588.
3   J. T. S. Irvine and P. A. Connor, in *Solid Oxide Fuel Cell: Facts and Figures*, eds. J. T. S. Irvine and P. Connor, Springer-Verlag, London, 2013, pp. 163–180.
4   A. Mai, F. Fleischhauer, R. Denzler and A. Schuler, *ECS Trans.*, 2017, **78**, 97–106.
5   P. Holtappels and U. Stimming, in *Handbook of Fuel Cells - Fundamentals, Technology and Applications*, eds. W. Vielstich, A. Lamm and H. A. Gasteiger, John Wiley & Sons, Chichester, UK, 1st edn., 2003, vol. 1, pp. 335–354.
6   C. Sun and U. Stimming, *J. Power Sources*, 2007, **171**, 247–260.
7   M. Cassidy, G. Lindsay and K. Kendall, *J. Power Sources*, 1996, **61**, 189–192.
8   M. Pihlatie, A. Kaiser and M. Mogensen, *Solid State Ionics*, 2009, **180**, 1100–1112.
9   T. Iwata, *J. Electrochem. Soc.*, 1996, **143**, 1521.
10   B. Iwanschitz, J. Sfeir, A. Mai and M. Schütze, *J. Electrochem. Soc.*, 2010, **157**, B269.
11   J. Kašpar, P. Fornasiero and N. Hickey, *Catal. Today*, 2003, **77**, 419–449.
12   R. Craciun, S. Park, R. J. Gorte, J. M. Vohs, C. Wang and W. L. Worrell, *J. Electrochem. Soc.*, 1999, **146**, 4019–4022.
13   S. P. Jiang, *Mater. Sci. Eng. A*, 2006, **418**, 199–210.
14   G. Corre, G. Kim, M. Cassidy, J. M. Vohs, R. J. Gorte and J. T. S. Irvine, *Chem. Mater.*, 2009, **21**, 1077–1084.
15   G. Corre, G. Kim, M. Cassidy and R. Gorte, *ECS Trans.*, 2009, **25**, 2201–2211.
16   M. C. Verbraeken, B. Iwanschitz, A. Mai and J. T. S. Irvine, *J. Electrochem. Soc.*, 2012, **159**, F757–F762.
17   T. Ramos, S. Veltzé, B. R. Sudireddy and P. Holtappels, *ECS Electrochem. Lett.*, 2014, **3**, F5–F6.
18   G. Kim, S. Lee, J. Y. Shin, G. Corre, J. T. S. Irvine, J. M. Vohs and R. J. Gorte, *Electrochem. Solid-State Lett.*, 2009, **12**, B48.
19   M. C. Verbraeken, B. Iwanschitz, E. Stefan, M. Cassidy, U. Weissen, A. Mai and J. T. S. Irvine, *Fuel Cells*, 2015, **15**, 682–688.
20   R. Kiebach, P. Zielke, J. V. T. Høgh, K. Thydén, H. J. Wang, R. Barford and P. V. Hendriksen, *Fuel Cells*, 2016, **16**, 80–88.
21   R. Price, M. Cassidy, J. A. Schuler, A. Mai and J. T. S. Irvine, *ECS Trans.*, 2017, **78**, 1385–1395.
22   R. Price, U. Weissen, M. C. Verbraeken, J. G. Grolig, A. Mai and J. T. S. Irvine, *ECS Trans.*, 2019, **91**, 1741–1750.
23   R. Price, M. Cassidy, J. A. Schuler, A. Mai and J. T. S. Irvine, *ECS Trans.*, 2015, **68**, 1499–1508.
24   R. Price, M. Cassidy, J. G. Grolig, A. Mai and J. T. S. Irvine, *J. Electrochem. Soc.*, 2019, **166**, F343–F349.
25   R. Price, M. Cassidy, J. G. Grolig, G. Longo, U. Weissen, A. Mai and J. T. S. Irvine, *Adv. Energy Mater.*, 2021, **2003951**, 1–21.
26   M. Schaffer, B. Schaffer and Q. Ramasse, *Ultramicroscopy*, 2012, **114**, 62–71.
27   M. R. Terner, J. A. Schuler, A. Mai and D. Penner, *Solid State Ionics*, 2014, **263**, 180–189.
28   S. Primdahl and M. Mogensen, *J. Electrochem. Soc.*, 1998, **145**, 2431–2438.
29   A. C. Müller, Karlsruhe Institute of Technology, 2004.
30   W. C. Chueh and S. M. Haile, *Phys. Chem. Chem. Phys.*,

2009, **11**, 8144–8148.

31 D. Burnat, G. Nurk, L. Holzer, M. Kopecki and A. Heel, *J. Power Sources*, 2018, **385**, 62–75.

32 J. Jamnik and J. Maier, *J. Electrochem. Soc.*, 1999, **146**, 4183–4188.

33 J. Jamnik and J. Maier, *Phys. Chem. Chem. Phys.*, 2001, **3**, 1668–1678.

34 C. Graves, C. Chatzichristodoulou and M. B. Mogensen, *Faraday Discuss.*, 2015, **182**, 75–95.

35 W. C. Chueh and S. M. Haile, *Annu. Rev. Chem. Biomol. Eng.*, 2012, **3**, 313–341.

36 S. Primdahl and M. B. Mogensen, in *Proceedings of the Fifth International Symposium on Solid Oxide Fuel Cells (SOFC-V)*, 1997, pp. 530–537.

37 R. Price, J. G. Grolig, A. Mai and J. T. S. Irvine, *Solid State Ionics*, 2020, **347**, 115254.

38 M. C. Verbraeken, B. Iwanschitz, E. Stefan, M. Cassidy, U. Weissen, A. Mai and J. T. S. Irvine, in *11th European SOFC and SOE Forum*, Lucerne, 2014, pp. 1–13.

39 P. A. Connor, X. Yue, C. D. Savaniu, R. Price, G. Triantafyllou, M. Cassidy, G. Kerherve, D. J. Payne, R. C. Maher, L. F. Cohen, R. I. Tomov, B. A. Glowacki, R. V. Kumar and J. T. S. Irvine, *Adv. Energy Mater.*, 2018, **8**, 1800120.

40 W. D. Kaplan, D. Chatain, P. Wynblatt and W. C. Carter, *J. Mater. Sci.*, 2013, **48**, 5681–5717.

41 D. Sarantaridis and A. Atkinson, *Fuel Cells*, 2007, **7**, 246–258.

42 A. Atkinson, S. Barnett, R. J. Gorte, J. T. S. Irvine, A. J. Mcevoy, M. Mogensen, S. C. Singhal and J. Vohs, *Nat. Mater.*, 2004, **3**, 17–27.

43 M. J. Jørgensen and M. Mogensen, *J. Electrochem. Soc.*, 2001, **148**, A433.